RSC Advances

PAPER

View Article Online
View Journal | View Issue

Cite this: *RSC Adv.*, 2022, **12**, 28937

Water-phase synthesis of Au and Au–Ag nanowires and their SERS activity

Ryota Kichijo,[a] Naoya Miyajima,[a] Daisuke Ogawa,[b] Hirokazu Sugimori,[b] Ke-Hsuan Wang,[a] Yoshiro Imura [a] and Takeshi Kawai *[a]

Received 1st September 2022
Accepted 6th October 2022

DOI: 10.1039/d2ra05496e

rsc.li/rsc-advances

Metal nanowires (NWs) with a diameter of a few nanometers have attracted considerable attention as a promising one-dimensional nanomaterial due to their inherent flexibility and conductive properties and their weak plasmon absorption in the visible region. In a previous paper, we reported the synthesis of ultrathin 1.8 nm-diameter Au NWs using toluene-solubilized aqueous solutions of a long-chain amidoamine derivative (C18AA). This study investigates the effect of different organic solvents solubilized in C18AA aqueous solutions on the morphology of the Au products and demonstrates that solubilizing methylcyclohexane yields thick 2.7 nm-diameter Au NWs and 3.3 nm-diameter Au–Ag alloy NWs. Further, the surface-enhanced Raman scattering sensitivity of ultrathin Au NWs, thick Au NWs, and thick Au–Ag alloy NWs were assessed using 4-mercaptopyridine and found that their enhancement factors are 10^4–10^5 and the order is Au–Ag NWs > thick Au NWs > ultrathin Au NWs.

1. Introduction

Shape controlled metallic nanocrystals have attracted attention because of their wide range of applications, including catalysis, electronics, photonics, and medicine.[1–8] As their morphology directly governs the physicochemical characteristics that determine the performance of the practical applications, precise morphological control of the metal nanocrystals is thus one of the fundamental research topics. Various shape-controlled nanocrystals, including thin plates, dendrimers, nanorods, and nanowires (NWs),[9–16] have been realized through advanced nanotechnology or wet-chemical methods. Among these metal nanocrystals, interest has recently been directed toward one-dimensional (1D) ultrathin metal NWs, as an emerging 1D nanomaterial, because of their inherent and unique optical, electrical, and mechanical properties.[17–24]

Concerning ultrathin metallic NWs, ultrathin Au NWs with a diameter <2 nm prepared using oleylamine in organic solvents have been exclusively investigated.[20–27] Au NWs, for example, have a characteristic surface plasmonic property and their longitudinal mode of the localized surface plasmon resonance appears as a broad band centered at approximately 20 μm.[28] Additionally, two-dimensional closely packed Au NWs can act as an excellent platform for surface-enhanced Raman scattering (SERS).[29,30] Further, their highly flexibility and transparency in the visible region allow flexible transparent electrodes to be prepared by densely depositing them on substrates.[4,31] Ultrathin Au NWs possess unique optical and electrical properties, hence the development of synthetic methods to produce Au NWs with different features, including diameters and branching structures, is an interesting challenge.

We previously reported that organogels composed of a long-chain amidoamine derivative (C18AA, Fig. 1a) can be employed as a soft-template for ultrathin Au NWs in the same approximately 2 nm size as those synthesized with oleyl-amine.[32–34] Further, we demonstrated that the water-phase synthesis of similar ultrathin Au NWs can be achieved by reducing $HAuCl_4$ in an aqueous C18AA solution with an appropriate amount of toluene,[35] whereas plate-like Au nanocrystals can be produced in the identical solution without toluene (Fig. 1b and c). The produced ultrathin Au NWs were covered with adsorbed C18AA layers, and the toluene dissolved in a bulk solution of C18AA naturally distributed into the layers. Since the distributed toluene influences the assembled structure of the adsorbed layers, that is, the molecular interaction between C18AA, the introduction of toluene induced a morphological transformation from plate-like nanocrystals to ultrathin NWs.[35]

It is readily conceivable that the solubilization of other solvents instead of toluene may have a different effect on the self-assembled layers of C18AA deposited on Au nanocrystals, allowing the possibility of preparing different types of Au nanocrystals. Herein, the effect of various organic solvents solubilized in aqueous C18AA solutions on the morphology of Au nanocrystals is investigated. We demonstrate that the addition of methylcyclohexane (MCH) allows thick and longer Au NWs with a narrow thickness size distribution to be prepared, and that MCH-containing C18AA aqueous solutions

[a]*Faculty of Engineering, Tokyo University of Science, 6-3-1 Niijuku, Katsushika-ku, 125-8585, Tokyo, Japan. E-mail: kawai@ci.tus.ac.jp*

[b]*Tokyo Metropolitan Industrial Technology Research Institute (TIRI), 2-4-10 Aomi, Koto-ku, 135-0064, Tokyo, Japan*

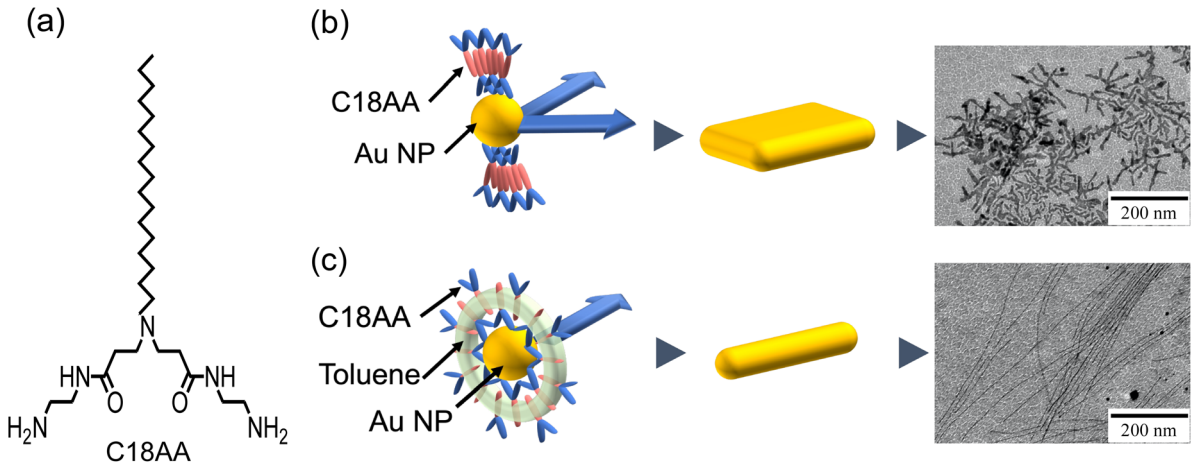

Fig. 1 (a) Molecular structure of C18AA. Schematic illustrating the formation of (b) plate-like Au nanocrystals with C18AA molecules in a C18AA solution without toluene and (c) ultrathin Au NWs in a C18AA solution with toluene.

are also effective for preparing thick Au–Ag bimetallic NWs. Furthermore, the performance of SERS on these NWs is discussed.

2. Experimental

2.1. Materials

Hydrogen tetrachloroaurate tetrahydrate ($HAuCl_4 \cdot 4H_2O$) was obtained from Nacalai Tesque, Japan. Silver nitrate ($AgNO_3$), toluene, MCH, lithium chloride, and hydrochloric acid were purchased from Kanto Chemicals, Japan. L-Ascorbic acid and 4-mercaptopyridine were purchased from Tokyo Chemical Industry, Japan. All chemicals were used as received. *N*-(2-Aminoethyl)-3-((2-(2-aminoethylcarbamoyl)ethyl)octadecylamino)propionamide (C18AA) was synthesized according to a previously reported procedure.[9]

2.2. Synthesis of ultrathin and thick Au NWs

Toluene (25.5 μL), for ultrathin Au NWs, and MCH (30.6 μL), for thick Au NWs, were added to an aqueous solution of 10 wt% C18AA (400 μL). After the mixture was homogenized using an ultrasonic homogenizer (45 kHz, 5 min), an aqueous solution of 20 mM $HAuCl_4$ (200 μL) was then added to the mixture. Additionally, a reducing-agent solution (200 μL) containing 60 mM L-ascorbic acid and 3 M lithium chloride was added to the mixture. The resultant solution was left to stand at 25 °C for 5 d.

2.3. Synthesis of Au–Ag alloy NWs

MCH (30.6 μL) was added to an aqueous solution of 10 wt% C18AA (400 μL), and the mixture was homogenized using an ultrasonic homogenizer (45 kHz, 5 min). After the pH of the mixture was adjusted using 0.5 M HCl or 0.5 M LiOH, aqueous solutions of 20 mM $HAuCl_4$ (100 μL) and 20 mM $AgNO_3$ (100 μL) were added to the mixture, and then a reducing-agent solution (200 μL) containing 60 mM L-ascorbic acid and 3 M lithium chloride was added to the mixture. The resultant solution was left to stand at 25 °C for 5 d.

2.4. Characterization

X-ray diffraction (XRD) measurements were performed using a diffractometer (Rigaku, Ultima IV). Transmission electron microscopy (TEM) images were acquired on a JEOL, JEM-1011 operating at 100 kV. High-resolution TEM (HR-TEM) images and TEM-energy dispersive X-ray spectra (TEM-EDS) were acquired using a JEOL, JEM-2100 operating at 200 kV. Raman spectra were obtained using a microscopic Raman spectrometer (JASCO, NRS-3200). The prepared ultrathin Au NWs, thick Au NWs, and thick Au–Ag alloy NWs were used as SERS platforms to detect 4-mercaptopyridine (4MPy) molecules with different concentrations. Briefly, aqueous solutions of 4.0×10^{-6} to 10^{-2} M 4MPy (10 μL) were added to the as-prepared NWs dispersions (90 μL). This solution was left to stand for 1 d to allow 4MPy to adsorb on the NW surfaces. 20 μL of each solution was dropped on CaF_2 substrates and dried in air. The diameter of the droplet was approximately 5 mm. The dried droplets were excited with a 785 nm laser at a power of 50 mW, and spectra were collected with an accumulation time of 10 s. The laser beam was focused on the sample using a × 2 objective lens, providing a scattering area of approximately 4 μm in diameter.

3. Results and discussion

3.1. Effect of solubilizing organic solvents on Au nanocrystals

We have previously reported that the solubilization of toluene into aqueous C18AA solutions yields 1.8 nm-diameter ultrathin Au NWs (Fig. 1c), and that plate-like Au nanocrystals were produced from the C18AA solutions without toluene (Fig. 1b).[35] The effect of various organic solvents, that is, *o*-, *m*-, and *p*-xylene, cyclohexane, carbon tetrachloride, ethylbenzene, benzene, mesitylene, and MCH, was investigated by reducing $HAuCl_4$ in C18AA solutions and solubilizing them. Fig. 2 clearly shows that the solubilization of other organic solvents, besides toluene, also has shaping effects on Au products. The resultant

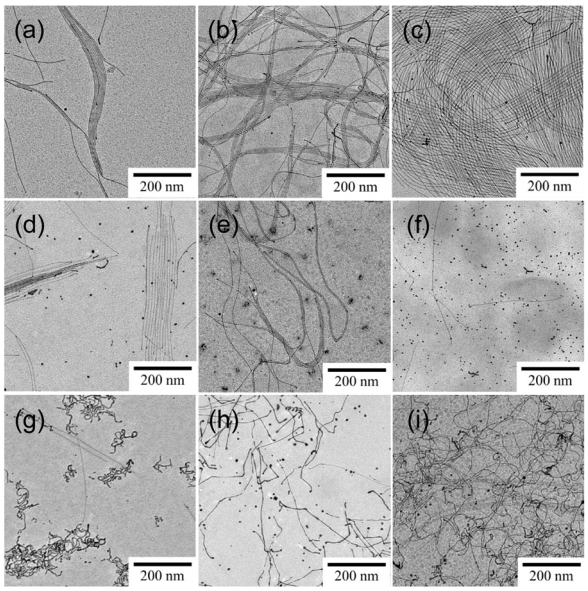

Fig. 2 TEM images of the Au nanostructures synthesized with (a) *o*-xylene, (b) *m*-xylene, (c) *p*-xylene, (d) ethylbenzene, (e) cyclohexane, (f) carbon tetrachloride, (g) mesitylene, (h) benzene, and (i) MCH.

products of all solvent systems were NWs and nanoparticles (NPs) as side products, but not the plate-like Au nanocrystals that were produced in C18AA aqueous solutions without organic solvent. This indicates that all solvents used here affected the Au nanocrystal morphology, although the length, diameters, and yield of the NWs depended on them. For example, ultrathin 2 nm-diameter Au NWs, which are the identical NWs produced in the toluene system (Fig. 1c), were obtained in the *o*-, *m*-, and *p*-xylene, cyclohexane, carbon tetrachloride, benzene, mesitylene, and ethylbenzene systems; however, the yield of ultrathin Au NWs in the cyclohexane, carbon tetrachloride, benzene, mesitylene, and ethylbenzene systems was very low due to the coexistence of many Au NPs. In contrast, solubilizing MCH yielded slightly thicker and longer Au NWs with homogeneous thicknesses, bending portions, and are different form the ultrathin Au NWs (Fig. 1c).

Fig. 3a shows the size distribution of the thick NWs, and the average diameter was calculated to be 2.7 ± 0.6 nm, which is approximately 1.5-fold larger than the 1.8 nm Au NWs prepared using toluene-solubilized aqueous solution of C18AA and oleylamine dissolved in organic solvents.[20–27,35] The XRD (Fig. 3b) and TEM-EDS (Fig. 3c) analyses confirmed that the thick NWs were Au. The peaks in the XRD spectrum at 38.3, 44.4, 64.6, and 77.6° were assigned to the (111), (200), (220), and (311) crystal facets of Au with a fcc structure, respectively.[29,35] Further, the HR-TEM image of the Au NWs (Fig. 3d) exhibited 0.235 nm periodic fringes on the Au (111) crystal facets in different directions, indicating that the thick NWs consisted of polycrystalline domains.[29,35] This polycrystalline feature was different from that of the 1.8 nm Au NWs consisting of a single crystalline domain (Fig. 3e). Hereafter, the NWs obtained from the toluene and MCH systems are described as ultrathin NWs and thick NWs, respectively.

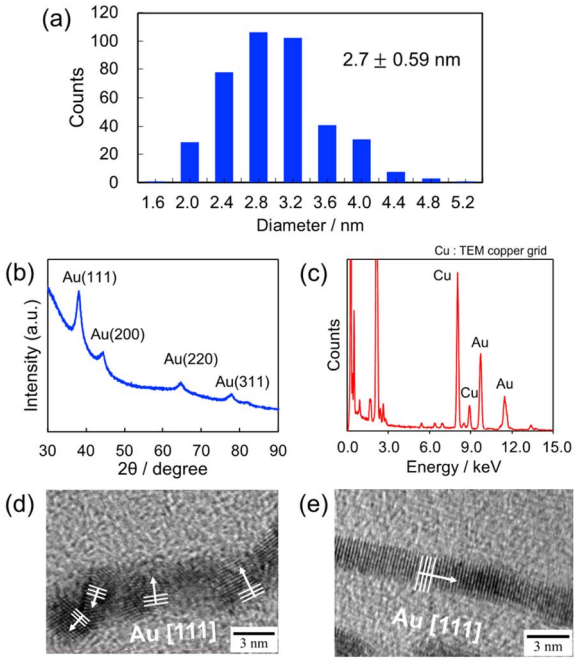

Fig. 3 (a) Diameter distribution, (b) XRD pattern, and (c) TEM-EDS spectrum of the thick Au NWs. Cu peaks are due to the copper mesh used as the substrate. HR-TEM images of (d) the thick Au NWs consisting of a polycrystalline domain and (e) the ultrathin Au NWs consisting of a single crystalline domain.

3.2. Synthesis of Au–Ag alloy NWs

The thick Au NWs can potentially be used as platforms for SERS because the bending portions may act as hot spots that strongly enhance Raman signals.[36–39] Silver and Au–Ag alloy, besides Au, are other highly suitable materials exhibiting a high SERS effect.[36,37,40–44] If thick Ag and Au–Ag alloy NWs can be fabricated using a similar procedure, they will be available as a high-performance platform for SERS detection. Hence, before evaluating the SERS activity of the thick Au NWs, we attempted to synthesize thick Ag and Au–Ag alloy NWs.

The same synthesis protocol used to produce thick Au NWs was applied to the MCH solubilized aqueous C18AA solution under the condition of fixing the total metal content while changing the ratio of Au to Ag. Fig. 4 shows TEM images demonstrating the effect of the Au/Ag loading ratio on the products. The images show that NWs were obtained for Au/Ag = 1 and 2, but not for Au/Ag = 0 and 0.5 with a high Ag content. Further attempts were made to synthesize Ag NWs under different conditions, including different organic solvents, precursor concentrations of Ag and C18AA, and temperature, but the synthesis of Ag NWs could not be achieved.

Au–Ag alloy NWs were definitely obtained at Au/Ag = 1 and 2, but many sea urchin-like aggregates were also observed as a by-product (Fig. 4e and f), indicating that further improvement of the preparation conditions is needed. Nouh *et al.* demonstrated with density functional theory calculations that the adsorption energy of the $NH_3^+Cl^-$ group on the surface of Au NWs is lower than that of the NH_2 group because $NH_3^+Cl^-$ groups form an

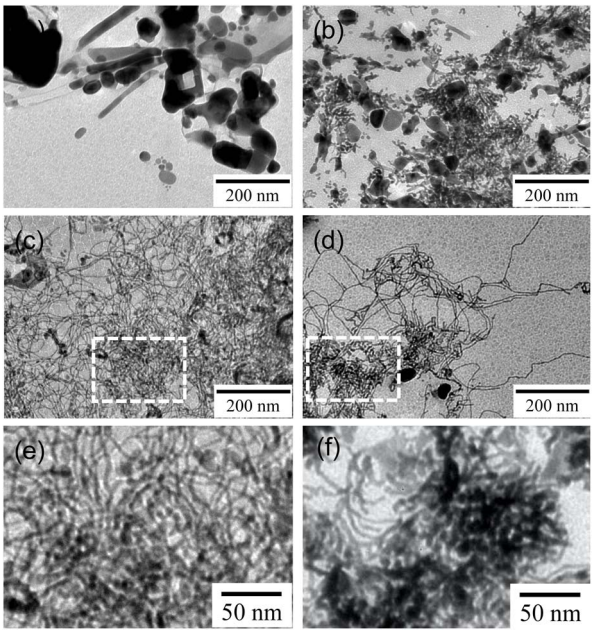

Fig. 4 TEM images of the Au–Ag nanocrystals prepared at an Au/Ag loading ratio of (a) 0, (b) 0.5, (c) 1, and (d) 2 in MCH solubilized aqueous solutions containing C18AA. (e and f) TEM images of the sea urchin-like aggregate surrounded by a white dotted line in (c) and (d).

ion pair network of NH_3^+ and Cl^- on the surface of Au NWs.[45] This effect is likely to be present in this study because the reaction solutions contain Cl^- originated from $AuCl_4^-$ and C18AA having such NH_2 groups as the terminal group (Fig. 1a). However, some of the terminal amine groups of C18AA are not protonated because the pH of the reaction solution was 9.4, slightly higher than the pH of 9.1 of C18AA,[46] and this effect seems not to work sufficiently. Hence, insufficient optimization of the conditions may lead to incomplete formation of such an ion-pair network. Ag–Au NWs were then prepared at different pH, and it was apparent that the pH value drastically affected the morphology of the products (Fig. 5). Alternatively, at pH =

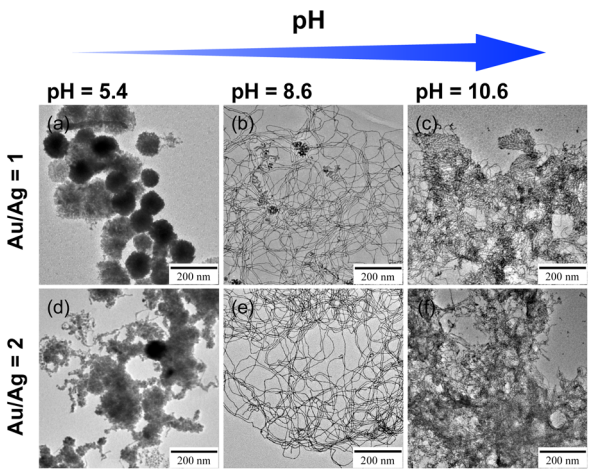

Fig. 5 TEM images of the Au–Ag nanocrystals with loading ratios of 1 and 2 synthesized in solutions with different pH.

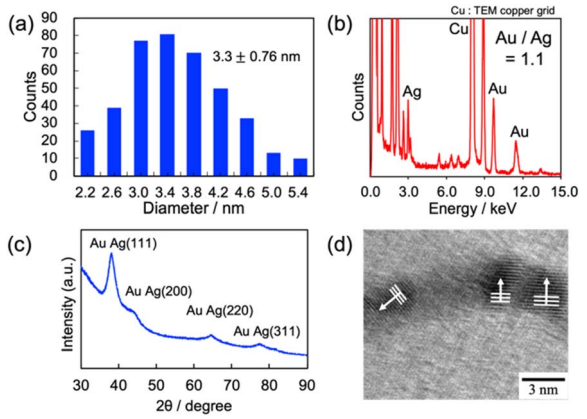

Fig. 6 (a) Diameter distribution, (b) TEM-EDS spectrum, (c) XRD pattern, and (d) HR-TEM images of the Au–Ag alloy NWs with an Au/Ag loading ratio of 1. White arrows indicate the directions of the (111) crystal facets in the domain.

8.6, longer NWs were produced without urchin-like aggregates, but no NWs were produced at a pH < 5.4 and >10.6, indicating that tuning the optimal pH is highly effective for facilitating the preparation of Ag–Au NWs.

Au–Ag alloy NWs prepared at an Au/Ag loading ratio of 1.0 were used for the SERS measurements. Fig. 6a shows the size distribution of the Au–Ag alloy NWs, and the average diameter was calculated to be 3.3 ± 0.8 nm. The composition of Ag–Au NWs was estimated to be Au/Ag = 1.08 ± 0.11 using the TEM-EDS measurements in Fig. 6b, which was approximately equal to the loading ratio ([Au]/[Ag] = 1.0) applied in the synthesis. Further, the XRD pattern in Fig. 6c suggests that the product was an alloy of Au and Ag, and the HR-TEM image of the Au–Ag alloy NWs (Fig. 6d) exhibited a typical polycrystalline structure consisting of 0.235 nm periodic fringes extending in different directions. The periodicity of the fringes corresponds to the (111) lattice spacing (0.237 nm) of the alloyed nanocrystals (Au/Ag = 1).[47,48] Accordingly, the morphology and polycrystalline structure of the thick Au and Au–Ag alloy NWs were similar.

3.3. SERS performance of Au and Au–Ag NWs

Ultrathin Au NWs are generally fragile and easily undergo morphological changes under the action of physico-chemical stimuli.[32,45,49] Hence, the adsorption of 4MPy, used as a probe for SERS measurements, may change the morphology of the NWs, resulting in a different SERS performance. Fig. 7 depicts TEM images of the ultrathin and thick Au NWs and Au–Ag NWs before and after 4MPy deposition. The images clearly show that the morphology of all the NWs was preserved even after the deposition of 4MPy.

Since the morphological change due to 4MPy deposition was demonstrated to be negligible, the SERS performance of each NW was accessed using these NW dispersions containing 4MPy. 20 mL of each NW dispersion containing a given concentration of 4MPy was dropped on CaF_2 substrates. The dispersions did not spread but adhered to the substrates as droplets with an approximate diameter of 5 mm, and the droplets dried in air

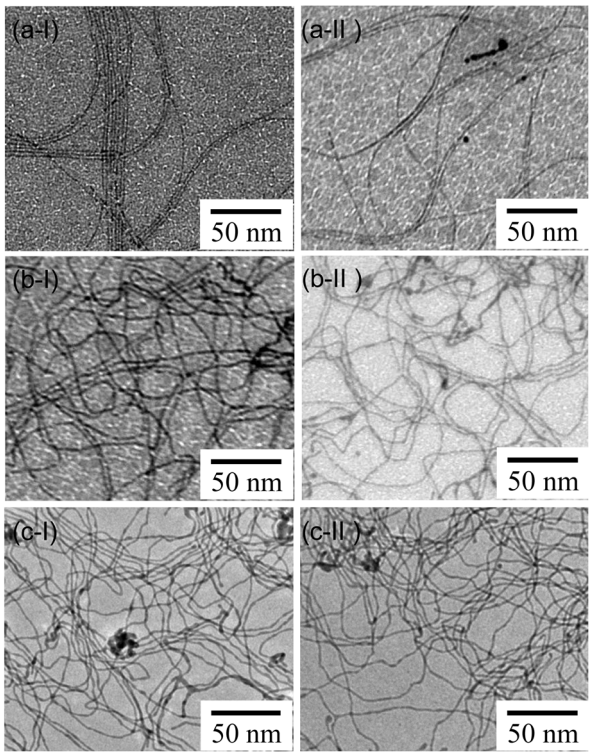

Fig. 7 TEM images of the (a) ultrathin Au NWs, (b) thick Au NWs, and (c) Au–Ag alloy NWs (I) before and (II) after 4MPy adsorption.

were subjected to Raman measurements. Fig. 8a shows the Raman spectra of 4MPy with different concentrations adsorbed on the thick Au NWs, together with 4MPy itself. The spectral feature was independent of the 4MPy concentration, and was identical to the previously reported SERS spectra of 4MPy deposited on Au NPs.[50,51] The strong bands at 426, 710, 1012, 1098, 1211, and 1575 cm^{-1} were assigned to the ring deformation, CH deformation, ring breathing, trigonal ring deformation, CH deformation, and C=C stretching modes, respectively.[52] The 4MPy Raman signals naturally increased with an increasing 4MPy concentration and could be detected even at a concentration of 4.0×10^{-6} M, that is, 4.1×10^{-12} M mm^{-2}. The enhancement factor (EF) of the thick Au NWs was estimated by comparing the Raman spectra of the thick Au NWs deposited with 4.0×10^{-5} M 4MPy and 0.10 M 4MPy without Au NWs. Considering the concentrations of 4MPy and the observed intensities of the ring breathing at 1012 cm^{-1} in Fig. 8a, the EF was calculated to be 7.7×10^4.

Further, Fig. 8b shows the SERS spectra of 0.04 mM 4MPy adsorbed on ultrathin Au NWs, thick Au NWs, and thick Au–Ag NWs. The thickness and the composition influenced the Raman intensity enhancement, but not on the spectral feature. The EFs of the ring breathing at 1012 cm^{-1} for the ultrathin Au NWs, thick Au NWs, and thick Au–Ag NWs were calculated to be 4.6×10^4, 7.7×10^4, and 33.0×10^4 (Fig. 8c), respectively, indicating that thicker NWs can serve as a high performance platform for SERS detection. Accordingly, the order of the enhancement was thick Au–Ag NWs > thick Au NWs > ultrathin Au NWs and

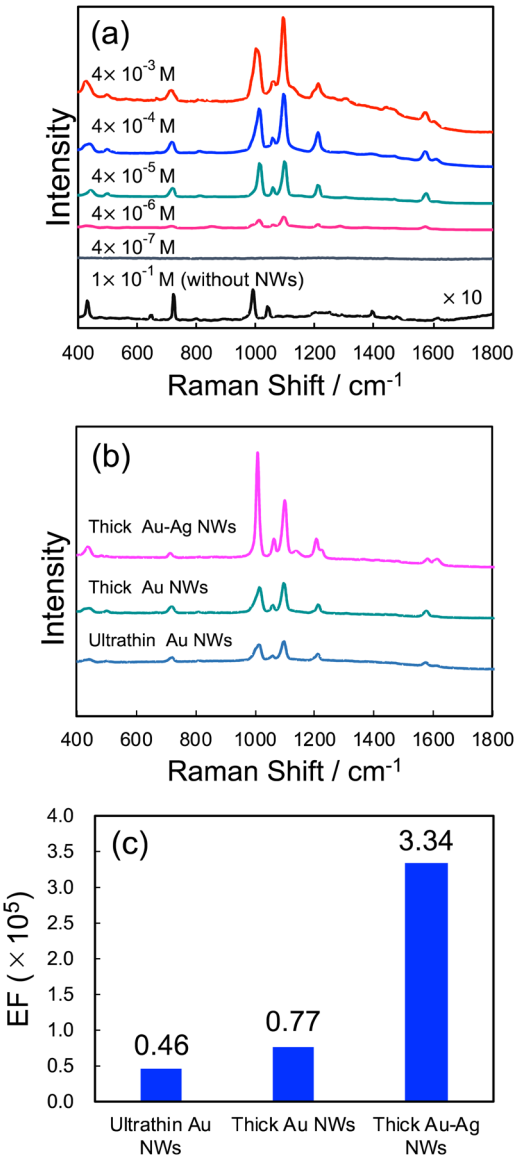

Fig. 8 (a) Raman spectra of the 4MPy adsorbed on thick Au NWs and a 4MPy of 1×10^{-1} M. The concentration of the 4MPy for adsorption was from 4×10^{-3} to 4×10^{-7} M. (b) SERS spectra of 4MPy adsorbed on ultrathin Au NWs, thick Au NWs, and thick Au–Ag NWs. The concentration of 4MPy was 4×10^{-5} M. (c) EFs of the ultrathin Au NWs, thick Au NWs, and thick Au–Ag NWs. The EF value was calculated using the 4MPy peak at 1012 cm^{-1} shown in (b).

alloying with Ag was found to be effective in improving SERS performance.

4. Conclusions

This study demonstrated that the morphologies of Au products in aqueous C18AA solutions were dependent on the types of the solubilized organic solvent, and that the solubilizing organic solvents play an important role in controlling the morphology of Au NWs. The solubilization of MCH yielded thick Au NWs with an approximate diameter of 2.7 nm, and the solubilization of MCH was also effective for synthesizing thick Au–Ag NWs.

The thick Au and Au–Ag NWs exhibited a polycrystalline structure with different crystal orientations, which was different from that of ultrathin Au NWs with a single crystal orientation. Additionally, thick Au and Au–Ag NWs can serve as high performance platforms for SERS detections.

Conflicts of interest

There are no conflicts of interest to declare.

Acknowledgements

This study was supported by JSPS KAKENHI (Grant No. 19K22116).

Notes and references

1 S. Cao, F. F. Tao, Y. Tang, Y. Li and J. Yu, *Chem. Soc. Rev.*, 2016, **45**, 4747–4765.
2 M. Jin, G. He, H. Zhang, J. Zeng, Z. Xie and Y. Xia, *Angew. Chem., Int. Ed.*, 2011, **50**, 10560–10564.
3 Y. Zhang, J. Guo, D. Xu, Y. Sun and F. Yan, *ACS Appl. Mater. Interfaces*, 2017, **9**, 25465–25473.
4 A. Sánchez-Iglesias, B. Rivas-Murias, M. Grzelczak, J. Pérez-Juste, L. M. Liz-Marzán, F. Rivadulla and M. A. Correa-Duarte, *Nano Lett.*, 2012, **12**, 6066–6070.
5 K. Saito and T. Tatsuma, *Nanoscale*, 2015, **7**, 20365–20368.
6 C. W. Hsu, B. Zhen, W. Qiu, O. Shapira, B. G. Delacy, J. D. Joannopoulos and M. Soljačić, *Nat. Commun.*, 2014, **5**, 3152.
7 X. Yang, M. Yang, B. Pang, M. Vara and Y. Xia, *Chem. Rev.*, 2015, **115**, 10410–10488.
8 Q. Tang, J. Liu, L. K. Shrestha, K. Ariga and Q. Ji, *ACS Appl. Mater. Interfaces*, 2016, **8**, 18922–18929.
9 Y. Imura, A. Maezawa, C. Morita and T. Kawai, *Langmuir*, 2012, **28**, 14998–15004.
10 S. E. Lohse, N. D. Burrows, L. Scarabelli, L. M. Liz-Marzán and C. J. Murphy, *Chem. Mater.*, 2014, **26**, 34–43.
11 B. An, M. Li, J. Wang and C. Li, *Front. Chem. Sci. Eng.*, 2016, **10**, 360–382.
12 G. Lin, W. Lu, W. Cui and L. Jiang, *Cryst. Growth Des.*, 2010, **10**, 1118–1123.
13 J. Gao, C. M. Bender and C. J. Murphy, *Langmuir*, 2003, **19**, 9065–9070.
14 T. Inaba, Y. Takenaka, Y. Kawabata and T. Kato, *J. Phys. Chem. B*, 2019, **123**, 4776–4783.
15 S. E. Lohse and C. J. Murphy, *Chem. Mater.*, 2013, **25**, 1250–1261.
16 X. Hong, C. Tan, J. Chen, Z. Xu and H. Zhang, *Nano Res.*, 2015, **8**, 40–55.
17 L. Cademartiri and G. A. Ozin, *Adv. Mater.*, 2009, **21**, 1013–1020.
18 R. Takahata and T. Tsukuda, *Chem. Lett.*, 2019, **48**, 906–915.
19 X. Teng, W.-Q. Han, W. Ku and M. Hücker, *Angew. Chem., Int. Ed.*, 2008, **47**, 2055–2058.
20 X. Lu, M. S. Yavuz, H.-Y. Tuan, B. A. Korgel and Y. Xia, *J. Am. Chem. Soc.*, 2008, **130**, 8900–8901.
21 B. Reiser, D. Gerstner, L. Gonzalez-Garcia, J. H. M. Maurer, I. Kanelidis and T. Kraus, *ACS Nano*, 2017, **11**, 4934–4942.
22 R. Venkatesh, S. Kundu, A. Pradhan, T. P. Sai, A. Ghosh and N. Ravishankar, *Langmuir*, 2015, **31**, 9246–9252.
23 C. Wang, Y. Hu, C. M. Lieber and S. Sun, *J. Am. Chem. Soc.*, 2008, **130**, 8902–8903.
24 A. Loubat, L.-M. Lacroix, A. Robert, M. Impéror-Clerc, R. Poteau, L. Maron, R. Arenal, B. Pansu and G. Viau, *J. Phys. Chem. C*, 2015, **119**, 4422–4430.
25 A. Halder and N. Ravishankar, *Adv. Mater.*, 2007, **19**, 1854–1858.
26 Z. Huo, C.-K. Tsung, W. Huang, X. Zhang and P. Yang, *Nano Lett.*, 2008, **8**, 2041–2044.
27 R. Takahata, S. Yamazoe, K. Koyasu, K. Imura and T. Tsukuda, *J. Am. Chem. Soc.*, 2018, **140**, 6640–6647.
28 R. Takahata, S. Yamazoe, K. Koyasu and T. Tsukuda, *J. Am. Chem. Soc.*, 2014, **136**, 8489–8491.
29 H. Feng, Y. Yang, Y. You, G. Li, J. Guo, T. Yu, Z. Shen, T. Wu and B. Xing, *Chem. Commun.*, 2009, 1984.
30 X. Hou, X. Zhang, S. Chen, Y. Fang, N. Li, X. Zhai and Y. Liu, *Colloids Surf., A*, 2011, **384**, 345–351.
31 Y. Chen, Z. Ouyang, M. Gu and W. Cheng, *Adv. Mater.*, 2013, **25**, 80–85.
32 Y. Imura, H. Tanuma, H. Sugimoto, R. Ito, S. Hojo, H. Endo, C. Morita and T. Kawai, *Chem. Commun.*, 2011, **47**, 6380.
33 C. Morita, H. Tanuma, C. Kawai, Y. Ito, Y. Imura and T. Kawai, *Langmuir*, 2013, **29**, 1669–1675.
34 C. Morita, C. Kawai, K. Tsujimoto, K. Kasai, Y. Ogue, Y. Imura and T. Kawai, *J. Oleo Sci.*, 2013, **62**, 81–87.
35 N. Miyajima, Y.-C. Wang, M. Nakagawa, H. Kurata, Y. Imura, K.-H. Wang and T. Kawai, *Bull. Chem. Soc. Jpn.*, 2020, **93**, 1372–1377.
36 S. Tiwari, A. B. Vasista, D. Paul, S. K. Chaubey and G. V. P. Kumar, *J. Phys. Chem. Lett.*, 2021, **12**, 6589–6595.
37 S. Roy, C. Muhammed Ajmal, S. Baik and J. Kim, *Nanotechnology*, 2017, **28**, 465705.
38 A. Dasgupta, D. Singh, R. P. N. Tripathi and G. V. P. Kumar, *J. Phys. Chem. C*, 2016, **120**, 17692–17698.
39 L. Vigderman and E. R. Zubarev, *Langmuir*, 2012, **28**, 9034–9040.
40 M. Fan, F.-J. Lai, H.-L. Chou, W.-T. Lu, B.-J. Hwang and A. G. Brolo, *Chem. Sci.*, 2013, **4**, 509–515.
41 J. Hu, B. Zhao, W. Xu, B. Li and Y. Fan, *Spectrochim. Acta, Part A*, 2002, **58**, 2827–2834.
42 K. Liu, Y. Bai, L. Zhang, Z. Yang, Q. Fan, H. Zheng, Y. Yin and C. Gao, *Nano Lett.*, 2016, **16**, 3675–3681.
43 Y. Cui, B. Ren, J.-L. Yao, R.-A. Gu and Z.-Q. Tian, *J. Phys. Chem. B*, 2006, **110**, 4002–4006.
44 L. Wang, H. Li, J. Tian and X. Sun, *ACS Appl. Mater. Interfaces*, 2010, **2**, 2987–2991.
45 E. S. A. Nouh, E. A. Baquero, L.-M. Lacroix, F. Delpech, R. Poteau and G. Viau, *Langmuir*, 2017, **33**, 5456–5463.
46 Y. Imura, K. Fukuda, C. Morita-Imura and T. Kawai, *ChemistrySelect*, 2016, **1**, 5404–5408.
47 H. Fu, X. Yang, X. Jiang and A. Yu, *Langmuir*, 2013, **29**, 7134–7142.

48 Y. Imura, T. Mori, C. M. Imura, H. Kataoka, R. Akiyama, H. Kurata and T. Kawai, *Colloids Surf., A*, 2018, **543**, 9–14.
49 Y. Imura, S. Hojo, C. Morita and T. Kawai, *Langmuir*, 2014, **30**, 1888–1892.
50 X.-S. Zheng, P. Hu, J.-H. Zhong, C. Zong, X. Wang, B.-J. Liu and B. Ren, *J. Phys. Chem. C*, 2014, **118**, 3750–3757.
51 X.-S. Zheng, P. Hu, Y. Cui, C. Zong, J.-M. Feng, X. Wang and B. Ren, *Anal. Chem.*, 2014, **86**, 12250–12257.
52 N. Wattanavichean, E. Casey, R. J. Nichols and H. Arnolds, *Phys. Chem. Chem. Phys.*, 2018, **20**, 866–871.